Volume 6
Number 11
7 June 2025
Pages 3357–3744

Materials Advances

rsc.li/materials-advances

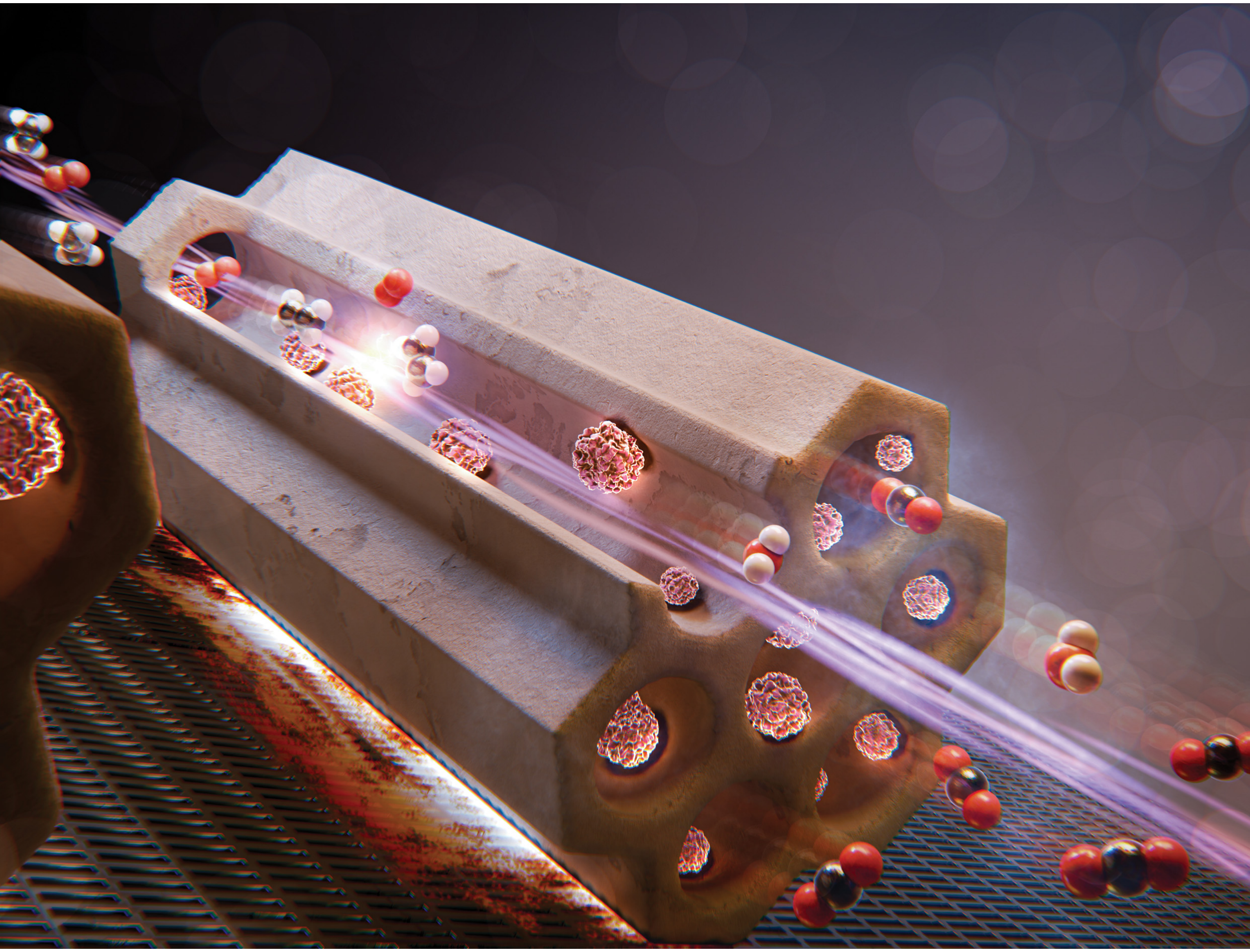

ISSN 2633-5409

ROYAL SOCIETY
OF **CHEMISTRY**

PAPER
Javier Ruiz-Martinez, Aamir Farooq *et al.*
Nano-confined manganese oxide on SBA-15 for ethylene catalytic oxidation

Materials Advances

ROYAL SOCIETY OF CHEMISTRY

PAPER

View Article Online
View Journal | View Issue

Check for updates

Cite this: *Mater. Adv.*, 2025, **6**, 3467

Nano-confined manganese oxide on SBA-15 for ethylene catalytic oxidation†

Mohamad Abou-Daher,[ab] Hassnain Abbas Khan,[a] Georgian Melinte,[c] Sarah Komaty,[b] Javier Ruiz-Martinez *[b] and Aamir Farooq *[a]

Received 12th December 2024,
Accepted 10th April 2025

DOI: 10.1039/d4ma01235f

rsc.li/materials-advances

This study investigates the synthesis and catalytic performance of nano-confined manganese oxide (MnO_x) on SBA-15 for ethylene oxidation. A "med-synthesis" approach, involving dry impregnation of manganese nitrate on as-synthesized SBA-15 *via* grinding, was employed to achieve high MnO_x loading and controlled dispersion within the mesoporous channels. The resulting catalysts (xMn/SBA-15_d) were characterized by XRD, SAXS, TEM, TGA, and XPS to understand the impact of MnO_x content on structural properties and catalytic activity. The results demonstrate that the dry impregnation method leads to well-dispersed MnO_x nanoparticles within the SBA-15 framework, even at high loadings (up to 30 wt%). In contrast, wet impregnation resulted in larger MnO_x particles and a loss of the ordered mesoporous structure. The nano-confined MnO_x particles exhibited excellent thermal stability, resisting sintering even after prolonged exposure to high temperatures (550 °C) under reaction conditions. Catalytic testing revealed that the 20 wt% Mn loaded on SBA-15 *via* the med-synthesis approach displayed superior activity for ethylene oxidation compared to the wet-impregnated counterpart, achieving complete conversion at lower temperatures. *In situ* TEM studies further confirmed the stability of the nano-confined MnO_x particles, highlighting the potential of this med-synthesis approach for developing highly active and durable catalysts for volatile organic compound oxidation.

1. Introduction

Volatile organic compounds (VOCs) are hazardous air pollutants emitted from both natural and anthropogenic sources. VOCs encompass various families of hydrocarbons, such as alkanes, alkenes, and aromatics.[1,2] Exposure to VOCs is a human health hazard because they are carcinogenic, teratogenic, toxic, and mutagenic.[3] Moreover, VOCs are also recognized as one of the primary drivers of photochemical smog, tropospheric ozone formation, and stratospheric ozone depletion.[4] Ethylene is one of the most studied VOCs in literature due to its harmful effects on humans and the environment. Numerous approaches have been explored and implemented to remove ethylene from industrial sources, including adsorption, incineration, and catalytic combustion.[4,5] This study selected ethylene as a model compound to represent the diverse range of hydrocarbons present in vehicle exhaust gases. As noted by Impens *et al.*,[6] the four most prevalent hydrocarbons in vehicle exhaust are typically ethylene (constituting 25 mol% of the total hydrocarbons), acetylene and methane (each accounting for 20 mol%), and aromatic compounds such as toluene (15 mol%) and benzene (5 mol%). Prior research demonstrates that ethylene exhibits reaction behavior comparable to that of toluene and benzene.[7,8] The key elimination methods to reduce VOC emissions at low concentrations and temperatures is the implementation of catalytic oxidation, which allows for the combustion of those hazardous compounds at lower temperatures compared to those required in gas phase reactions. The design of the catalytic material is the key step in guaranteeing efficient VOC removal.[1,2,9,10] The catalytic active material can consist of two main classes: noble and non-noble metal-based catalysts. Non-noble metals are characterised by their good activity in VOC oxidation due to their high stability, poison resistance, wider availability and lower cost compared to noble metals.[11,12]

Transition metal oxides are widely studied in the literature for hydrocarbon oxidation.[12] Among these, manganese oxide-based catalysts are reported to be among the most efficient transition metal compounds for oxidation catalysis, and they are environmentally friendly as well.[13] However, the catalytic performance of MnO_x nanoparticles as oxidation catalysts has not been fully recognized. In particular, little attention has

---

[a] Clean Energy Research Platform, Physical Sciences and Engineering Division, King Abdullah University of Science and Technology (KAUST), Thuwal 23955-6900, Saudi Arabia. E-mail: aamir.farooq@kaust.edu.sa

[b] KAUST Catalysis Center, Physical Sciences and Engineering Division, King Abdullah University of Science and Technology (KAUST), Thuwal 23955-6900, Saudi Arabia. E-mail: javier.ruizmartinez@kaust.edu.sa

[c] Imaging and Characterization Lab, King Abdullah University of Science and Technology (KAUST), Thuwal 23955-6900, Saudi Arabia

† Electronic supplementary information (ESI) available. See DOI: **https://doi.org/10.1039/d4ma01235f**

been paid to the catalytic behaviour of MnO_x catalysts in oxidation/combustion reactions at low temperatures (*e.g.*, below 300 °C), which are usually performed with noble metal catalysts.[14–17] Generally, the catalytic activities of transition metal oxide catalysts are lower than those of noble metal catalysts. However, the inherent advantages of metal oxide catalysts, such as low cost, high thermal stability, and high mechanical strength, make them a promising alternative in several catalytic applications.[18,19] Therefore, the controlled synthesis of MnO_x nanomaterials has attracted considerable attention from both academia and industry perspective.[20–22] Recently several reports on dry impregnation of metal precursors have achieved high dispersion with well-controlled particle size.[23] Generally, inorganic precursors are first introduced into the channels of host materials, such as mesoporous silica, and then metal precursors are calcined to produce metal nanoparticles with replicas of the confined space.[24,25] Several mesoporous materials like CeO_2 and ZrO_2 have been used; however, due to their low surface area, their performance remains less attractive.[26,27]

Since the first synthesis of SBA-15 by Zhao *et al.*[28] with a hexagonal pore network, the tuneable pore size has facilitated the accommodation of larger molecules, mitigating mass transfer limitations compared to other conventional metal oxides. Therefore, the inert nature and inherent hydrophobic properties of SiO_2 make mesoporous SBA-15 a promising support material for the incorporation of various active compositions.[29,30] Extensive research efforts have gone into the modification of silica-based materials with active nanoparticles, with two main strategies for the synthesis of silica supported materials: the "one-pot" method (or pre-synthesis method) and the "loading" method (or post-synthesis method).[31] With the "one-pot" method, the silicon source and the active metal precursor are mixed, and they subsequently interact with the template to form a porous framework. This method is simple and results in an atomic-level mixture of active sites within the porous material. However, adding extra heteroatoms to the framework could disrupt the ordered mesoporous structure and cause further collapse during calcination.[32–34] The "loading" method mainly involves first preparing a stable mesoporous silica matrix and then adding the active component to it ref. 35–37. Several variations of this strategy have been reported in literature including impregnation,[14] deposition–precipitation,[38] graft hybrid,[39] colloidal immobilization,[40] and vacuum calcination.[41] A notable challenge with this method is the distribution of active species, such as nanoclusters of metals or metal oxides, within the elongated pore channels. This distribution may be susceptible to sintering effects during high-temperature calcination. Moreover, achieving high metal loading inside the channels of SBA-15 remains challenging.[42]

An intriguing alternative is the "med-synthesis" approach, positioned as an intermediate method between pre- and post-synthesis techniques. In this approach, denoted as med-synthesis, the template is retained within the pores. Med-synthesis holds the potential to amalgamate the advantages of both pre- and post-synthesis approaches. This includes achieving a well-distributed active phase and maintaining a defined structure, offering a promising compromise in the realm of porous material synthesis. In their earlier work, Zhu and Sun's group[43,44] reported the existence of extraordinarily confined spaces between the silica walls in the as-synthesized SBA-15 (as-SBA-15). By efficiently utilizing this space, a high degree of monolayer dispersion of active metal oxides with high loading can be achieved. The nanoconfinement of metals within SBA-15 pores *via* the "med-synthesis approach" is accomplished by dry impregnation of metal precursor over as-SBA-15 *via* grinding. This method employs pluronic P-123 in as-SBA-15 as a surfactant to assist in impregnation and agglomeration prevention[24,31,45,46]

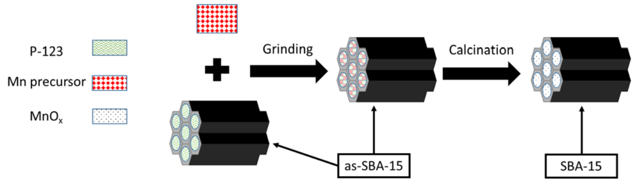

Scheme 1 Synthesis process for mesoporous silicate loaded with MnO_x *via* the med-synthesis approach.

The incorporation of high metal loading opens the door for the utilization of transition metal oxides as an economical alternative to noble metals such as Pt which is considered an optimal catalyst for hydrocarbon oxidation applications.[42,47]

In this study a manganese precursor was directly incorporated into as synthesized SBA-15 by employing the med-synthesis approach using solid state grinding of the precursor (Scheme 1). The subsequent calcination in air was conducted to obtain the resultant material which where denoted as (xMn/SBA-15_d). Manganese nitrate was used in the preparation of the supported systems due to the ease of removing nitrates anions during the calcination. The best performing catalyst prepared *via* dry impregnation was benchmarked against manganese oxide catalysts synthesized by the wet impregnation method. The controlled crystal growth has gained significant attention for several oxidation reactions, specifically low temperature CO and hydrocarbon oxidation,[48–50] and in this context, this work investigates synthesis of MnO_x on SBA-15 support by controlled dispersion. This study also aims to enhance the understanding of the catalyst structure, dispersity, and catalytic properties of MnO_x nanoparticles for ethylene oxidation, which is crucial for mitigating the impact of unburned hydrocarbons on global warming.

2. Experiment

2.1 Materials

Manganese(II) nitrate hydrate ($Mn(NO_3)_2{\cdot}xH_2O$), tetraethyl orthosilicate (TEOS, 98%), hydrochloric acid (HCl, 37%), and Pluronic P-123 ($EO_{20}PO_{70}EO_{20}$, M_n = ∼5800) were purchased from Sigma-Aldrich.

2.2. Catalyst synthesis

2.2.1 Synthesis of SBA-15. The well-known synthesis procedure was adopted from the literature.[15,51] Briefly, 4.0 g of P-123 were dispersed overnight in 110 ml of DI water. 20 ml of

HCl are then added over the P-123 solution and left to stir for 20 min. The solution temperature is elevated to 36 °C and then 8 g of TEOS are added dropwise and the mixture is kept stirring for 4 hour. The formed suspension is hydrothermally treated at 130 °C for 16 hour. The precipitated material is collected and dried at 80 °C overnight. The dried precipitate is denoted as as-SBA-15.

2.2.2 Dry impregnation to synthesize *x*Mn/SBA-15 catalyst. Manganese(II) nitrate is dry impregnated over as-SBA-15 by grinding both solids well for 30 min as demonstrated in Scheme 1. The manganese precursor weight is adjusted to produce the following weight percentages respectively: 10, 15, 20, 25, and 30 wt%. The solid mixture is then calcined at 550 °C for 6 hour at 1 °C min^{-1} and left to cool naturally. The produced catalysts are denoted as 10Mn/SBA-15_d, 15Mn/SBA-15_d, 20Mn/SBA-15_d, 25Mn/SBA-15_d, and 30Mn/SBA-15_d respectively.

2.2.3 Wet impregnation to synthesize 20Mn/SBA-15 catalyst. For the preparation of the wet impregnated catalyst, $Mn(NO_3)_2\cdot xH_2O$ is dissolved in 100 ml of DI water. The precursor corresponding to 20 wt% is mixed well, and SBA-15 support recovered after calcination is added for impregnation. The rotary evaporator was used to desiccate the sample and dry it in vacuum. After the solvent is completely dried, the sample was dried for 12 hour at 80 °C and calcined at 550 °C for 6 hour. Temperature was ramped from room temperature to 550 °C with 1 °C min^{-1}. The sample is denoted as 20Mn/SBA-15_w.

2.3 Characterization

Crystal structure of the catalyst was characterized by powder X-ray diffraction (XRD) on a Bruker D8 Advance using Cu k_α radiation source with a wavelength of 1.5418 Å at 40 kV and 40 mA in the range of 10–90°. The same instrument was used for small-angle X-ray scattering (SAXS).

Analyzer 5500 (TA Instruments, US) was used to analyze thermogravimetric (TGA) properties of the samples. Measurements were conducted under an air atmosphere with a flow rate of 20 ml min^{-1}. The samples used had an approximate mass of 4.0 mg.

Textural properties of the catalyst were evaluated by N_2 physisorption in Micromeritics ASAP-2020 equipment. Catalysts (300 mg) were first degassed for 5 h at 150 °C. Specific surface area was calculated in the relative pressure range of 0.01–0.2, assuming the N_2 molecule has a cross-sectional size of 0.162 nm^2.

Catalyst morphology was probed using a TEM Titan Themis microscope. To record the *in situ* evolution of MnO_x particles with temperature, K3 direct detection camera was used. Surface compositions and chemical states were analyzed by X-ray photoelectron spectroscopy on a XPS Amicus. High-resolution X-ray photoelectron spectroscopy (HrXPS) using a Kratos Axis Ultra photoelectron spectrometer (Kratos Analytical Ltd) was employed to analyze the chemical bonding states of the FAC anodes. Prior to analysis, the samples underwent Ar^+ ion beam etching for a duration of 30 minutes. The HrXPS measurements were conducted using a Kratos Axis Ultra DLD spectrometer with a monochromatic Al K X-ray source, operating at 150 W and an energy of $h\nu$ = 1486.6 eV. The spectrometer was equipped with a multichannel plate, delay line detector, and maintained a vacuum level of 1×10^{-8} mbar. The entire survey spectra and high-resolution spectra were acquired at fixed analyzer pass energies of 160 and 20 eV, respectively. The binding energies were calibrated using the C 1s peak set at 284.8 eV. Analysis of the XPS spectra was performed using CasaXPS, a commercially available software. The fitting method described by Biesinguer *et al.*[52] was employed for spectrum analysis, and a Shirley background was applied to the Mn $2p_{3/2}$ region.

Mn loading in the prepared catalysts is quantified using a wavelength dispersive XRF spectrometer (Bruker S8 TIGER WD-XRF).

2.4 Catalytic testing

Catalytic testing was performed in a U-shaped reactor. For each test 30 mg of pelletized catalyst (45–60 mesh) were loaded into the reactor and sandwiched between two layers of glass wool. The reactor bed was heated by an electric oven and a k-type thermocouple touching the catalyst bed was used for temperature measurement. The inlet feed consists of 850 ppm ethylene, 15% oxygen, and balance nitrogen. The gas hourly space velocity is 64 000 ml g_{cat}^{-1} h^{-1}. Agilent gas chromatograph (7890 B) with FID and TCD detectors was used to monitor the reactant concentration. Ethylene conversion is defined as:

$$\text{Conversion}\% = \frac{X_{\text{Ethylene}}(\text{initial}) - X_{\text{Ethylene}}(\text{final})}{X_{\text{Ethylene}}(\text{initial})} \times 100\%$$

To evaluate the apparent rate constant, calculations were performed under the following assumptions:

(1) The rate expression is assumed to be first order power law that is dependent on ethylene partial pressures, *i.e.*, $r = kP_{C_2H_4}$.

(2) The occurring reaction is assumed to be complete combustion.

(3) Atmospheric pressure, isobaric conditions, throughout the catalyst bed.

(4) Isothermal conditions throughout the catalyst bed.

(5) The change in total molar flow rate (F_{total}) is negligible since the ethylene stream is diluted ($\leq$1% C_2H_4 in all cases).

(6) The absence of heat and mass transfer limitations and other parasitic phenomena.

To derive the expression of the rate constant, the change in the molar flow rate of ethylene with respect to catalyst loading is expressed as:

$$\frac{dF_{C_2H_4}}{dW} = -kP_{C_2H_4}$$

where $F_{C_2H_4} = Q\cdot C_{C_2H_4}$, $C_{C_2H_4} = \frac{P_{C_2H_4}}{RT}$, $Q = Q^0\frac{T}{273.15}$ (to account for flow expansion with temperature). Thus $F_{C_2H_4} = Q\frac{P_{C_2H_4}}{R\cdot T}$ and $\frac{dF_{C_2H_4}}{dW} = \frac{Q}{R\cdot T}\frac{dP_{C_2H_4}}{dW} = \frac{1}{R\cdot 273.15}\frac{dP_{C_2H_4}}{d\tau}$, where R is the gas constant $\left(R = 8.2\times10^{-5}\left[\frac{\text{m}^3\ \text{atm}}{\text{mol K}}\right]\right)$ τ is the catalyst weight-to-volumetric flow rate ratio $\tau = \frac{W}{Q^0}\left[\mathrm{g\ s\ m^{-3}}\right]$. The change in molar flow rates of ethylene with respect to conversion (X) is expressed as $F_{C_2H_4} = F^0_{C_2H_4}(1-X)$. The partial pressure is calculated as $P_i = \frac{F_i}{F_{\mathrm{total}}} \cdot P^0 = y_i \cdot P^0$. Thus, the rate constant is calculated by fitting a kinetic integral model over the bed loading *via* the following expression:

$$k = \frac{1}{R \cdot 273 \cdot \tau} \ln\left(\frac{1}{1-X}\right)$$

To investigate water resistance of the optimum dry impregnated catalyst and its wet-impregnated counterpart, tests were conducted under wet feed conditions. The inlet feed for these tests consisted of 850 ppm ethylene, 15% oxygen, 5% water vapours, and balance nitrogen. The gas hourly space velocity was maintained at 64 000 ml $\mathrm{g_{cat}}^{-1}$ h^{-1}.

To investigate the thermal stability, the catalyst was exposed to elevated temperatures for 6 hours under reaction flow conditions. After keeping the catalyst under isothermal conditions for 6 hours, it was cooled down to 125 °C and the catalytic testing was performed by incrementing the temperature gradually until complete conversion was attained. Two tests were performed in the case of 20Mn/SBA-15$_d$ samples, where their catalytic performance was evaluated after their exposure to reaction flow conditions at 550 °C and 625 °C. For the case of 20Mn/SBA-15$_w$, it was exposed to 550 °C. Moreover, time-on-stream stability test for 100 hours was performed for the best performing catalyst (20Mn/SBA-15$_d$) at 225 °C.

3. Results and discussion

Fig. 1 shows the X-ray diffraction patterns of the SBA-15 support and metal-loaded catalysts with different loading concentrations. The wider peak appearing at 22.6° corresponds to amorphous SiO_2. The catalysts loaded up to 15 wt% did not show a well observed crystal structure of MnO_x, indicating that the metal oxide is well dispersed. As shown in Fig. 1, the main crystalline structures of Mn in the 10–30 wt% Mn/SBA-15 samples after calcining were Mn_2O_3 (89-4836) and MnO_2 (89-5171). This suggests that the amorphous MnO_x crystalize to MnO, MnO_2 and Mn_2O_3 at 550 °C. It is worth noting that the crystal size in the case of wet impregnated catalyst is greater. We hypothesize that in wet impregnation particles grow on the unprotected SBA-15 surface. Consequently, these particles begin to sinter when calcined at higher temperatures (550 °C). However, in dry impregnation, MnO_x crystals are nanoconfined within SBA-15 pores.

The SAXS patterns displayed in Fig. 2 illustrate the distinctive features of the dry impregnated and pristine SBA-15 samples. The appearance of three diffraction peaks within the range of $2\theta = 0.4°–3°$ provides evidence for the development of neatly arranged hexagonal pores. Specifically, these peaks correspond to the (100), (110), and (200) planes, which are indicative of the well-defined hexagonal (*p*6*mm*) pores found in SBA-15.[53,54] These distinctive features of ordered pores are absent in the case of the wet-impregnated sample.

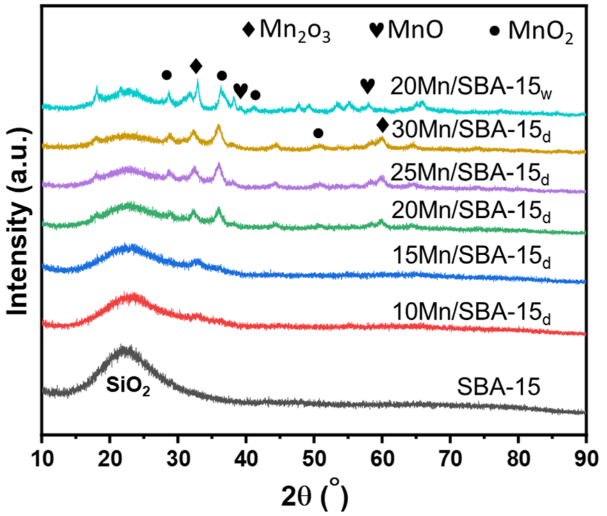

Fig. 1 X-ray diffraction patterns of all the MnO_x/SBA-15 prepared catalysts.

Fig. 3 shows thermogravimetric analysis (TGA) curves of the polymers P-123 which is used as a template for SBA-15. In the TGA curve for P-123, weight loss started sharply at around 50 °C and was complete at 250 °C. The observed thermal decomposition of bare as-made SBA-15 shows a single weight loss of 47 wt% at about 120 °C, which is associated with the decomposition of the triblock copolymer P-123 slightly embedded in the siliceous pore walls. We identified 221 °C as a critical temperature point, attributed to the onset of manganese nitrate decomposition. Weight losses observed below 221 °C are assigned to the release of surface and structural water, while at temperatures above 221 °C the decomposition of nitrate resulted in the release of NO_x gas and a further substantial

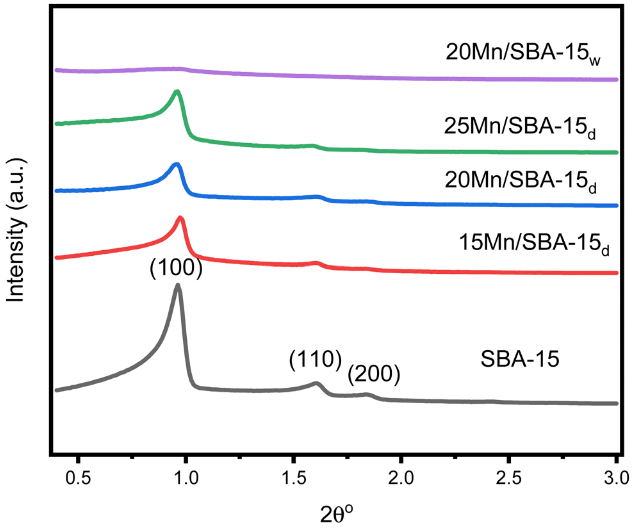

Fig. 2 SAXS patterns depicting the structural features of pristine SBA-15 and Mn-loaded SBA-15 samples at various manganese loading levels.

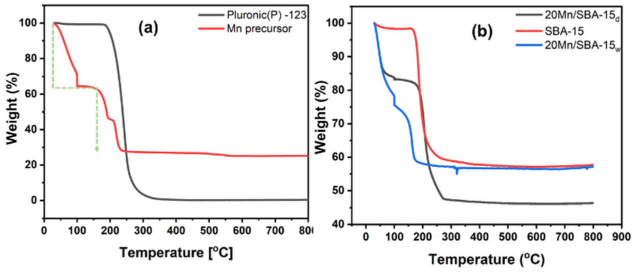

Fig. 3 TGA curves of (a) P-123 template and $Mn(NO_3)_2{\cdot}xH_2O$ and (b) TEOS condensed on P-123, and 20 wt% Mn loaded on SBA-15 at a heating rate of 10 °C min^{-1}.

weight loss of 35 wt%. Sample 20Mn/SBA-15_w calcined in air shows a substantial decrease in weight below 200 °C due to lower onset temperatures for the release of water and manganese nitrate decomposition compared to bare manganese nitrate.

N_2 adsorption and desorption isotherms were measured on all samples to evaluate the surface and structural properties. The N_2 adsorption curves are presented in Fig. 4, and the data are summarized in Table 1.

Both pure SBA-15 and xMn/SBA-15_d samples exhibited adsorption isotherms of type IV with hysteresis loops, which are characteristic of nanostructured materials with uniform mesopores. The adsorption and desorption isotherms showed a large increase in the relative pressure (P/P_0) ranging from 0.6 to 0.8 for SBA-15 and from 0.5 to 0.7 for MnO_x on SBA-15, which is caused by capillary condensation into the mesopores. N_2 adsorption data presented in Fig. 4(a).

Table 1 show that the pore diameter and surface area comparison of the prepared catalysts. The specific surface area of SBA-15 was found to be 518 m^2 g^{-1}. The surface of catalyst (xMn/SBA-15_d) after calcination decreased up to 340 m^2 g^{-1} for 30Mn/SBA-15_d which is the highest loading in dry impregnation method. The highest decrease in area is noted for catalyst prepared by wet impregnation, indicating that the pores were progressively blocked by MnO_x nanoparticles. In contrary to dry impregnated samples wet, impregnated one exhibited adsorption isotherms of type type III, which indicates the loss of ordered mesoporosity, which is in accordance with SAXS resultshe BJH pore size distribution (Fig. 4b) reveals a monomodal distribution for both SBA-15 and the dry-impregnated catalyst. In contrast, the wet-impregnated sample exhibits a bimodal distribution, indicating the presence of pores both on the surface and within the silica support.[55]

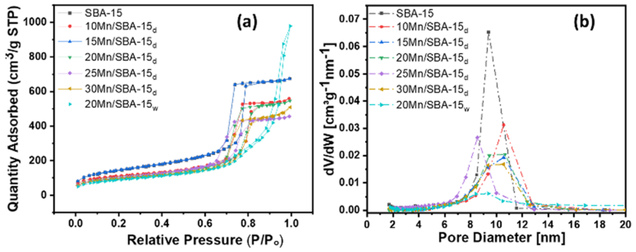

Fig. 4 (a) N_2 adsorption desorption isotherm (b) BJH pore size distribution of prepared catalysts.

Table 1 BET surface area and pore size calculated from BJH pore size distribution

Catalyst	Surface area [m^2 g^{-1}]	Pore size [nm]
SBA-15	518	8.5
10Mn/SBA-15_d	397	10.2
15Mn/SBA-15_d	358	9.8
20Mn/SBA-15_d	361	9.7
25Mn/SBA-15_d	354	9.9
30Mn/SBA-15_d	340	10.3
20Mn/SBA-15_w	320	20.4

TEM observation results and EDS mapping of xMn/SBA-15 under vacuum conditions are shown in Fig. 5. It is remarkable that MnO_x up to 20% did not grow significantly in size due to the nanoconfinement inside the porous walls of SBA-15. In the wet impregnation method, the particles are mostly on the surface and are not strongly encapsulated by thick walls. EDX mapping analysis was used to test the elemental dispersion of xMn/SBA-15_d composites (see Fig. 5). The mapping images of 15–25Mn/SBA-15_d demonstrated that Mn element was uniformly distributed on SiO_2 after calcination. The xMn/SBA-15_d composites have a stable structure under 550 °C. The effect was attributed to the interaction between SBA-15 and MnO_x as well as the channel limiting effect.

The comparison for the manganese oxide particle size distribution of dry impregnated 20Mn/SBA-15_d and wet impregnated catalyst 20Mn/SBA-15_w is given in Fig. 6 with average particle size of 7.3 nm and 48 nm, respectively. The growth of particle in wet impregnation implies that the particles are already sintered when calcined at high temperature (550 °C) for the activation of the catalyst. In case of dry impregnation, the particles are not sintered, rather they remained intact.

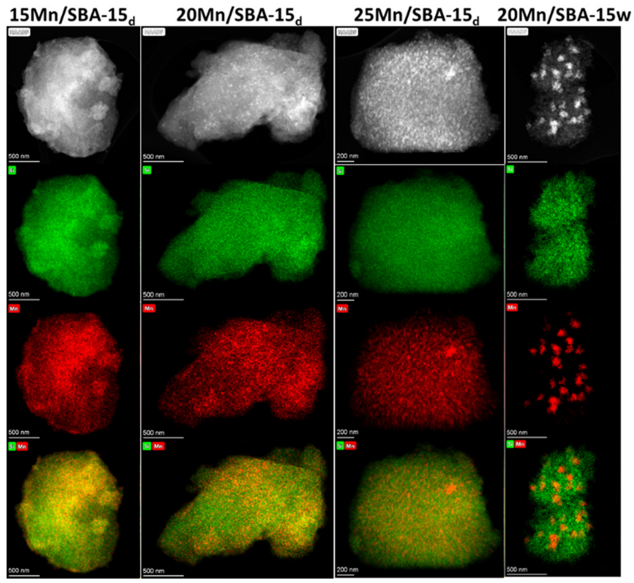

Fig. 5 TEM and EDX color mapping of catalysts prepared with dry and wet impregnation methods.

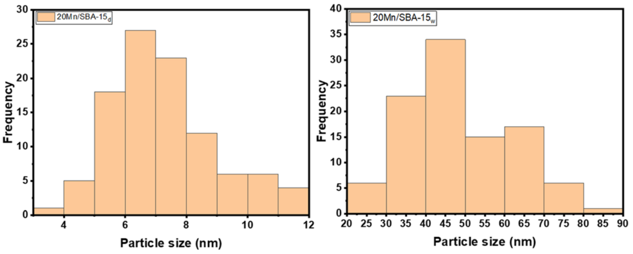

Fig. 6 Average particle size distribution calculated for 20Mn/SBA-15$_d$ and 20Mn/SBA-15$_w$.

To investigate sample stability under reaction conditions, TEM results for spent catalysts are reported in Fig. 7. The spent catalyst 20Mn/SBA-15$_d$ in Run-1 shows a slight increase in particle size after 6 hours at 550 °C as the average particle size is 10 nm. However, after exposure to reaction conditions in Run-2 at 625 °C for 6 hours, the average particle size of 20Mn/SBA-15$_d$ increased to 16.7 nm, which gives an indication on the thermal stability limit of this catalyst. In the case of wet impregnated sample, the average particle size increased after Run-1 from 48 nm to 54.1 nm. The average particle size distribution for the spent catalysts is reported in Fig. S1 (ESI†).

Since atomic movement is easily influenced by temperature and partial pressure of gas surrounding the sample, adjusting the reaction temperature can change atomic dispersion and modify catalyst surface defects, thereby affecting reactivity. We utilized *in situ* TEM to investigate the behavior of MnO_x particles under controlled gas conditions and temperature variations. The dynamic evolution process of uncalcined 20Mn/SBA-15$_d$ catalyst under increasing temperature and switching oxygen/nitrogen conditions was monitored with TEM measurements. In Fig. 8, TEM measurements are taken at conditions closely resembling air conditions: 80% N_2 with 20% O_2 at a total flow rate of 1 ml min^{-1}. Pressure was maintained at 1 atm, and temperature was ramped from 175 to 625 °C with a ramping rate of 1 °C min^{-1} and intermediate temperature intervals of 350, 450, and 550 °C.

When the temperature was systematically increased from 175 to 625 °C, MnO_x particles remained elusive until the temperature reached 625 °C. This observation indicates a temperature threshold for the appearance of MnO_x particles in the given conditions (shown in the inset of Fig. 8). Further investigation involved continuous heating at 550 °C for 60 minutes, during which TEM images were captured. Surprisingly, despite the prolonged heating, there was no discernible evolution of particles from the MnO_x material.

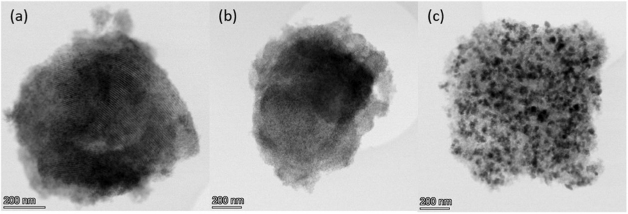

Fig. 7 TEM images of spent catalysts after thermal stability catalytic testing: (a) 20Mn/SBA-15$_d$ at 550 °C, (b) and 625 °C, (c) 20Mn/SBA-15$_w$ at 550 °C.

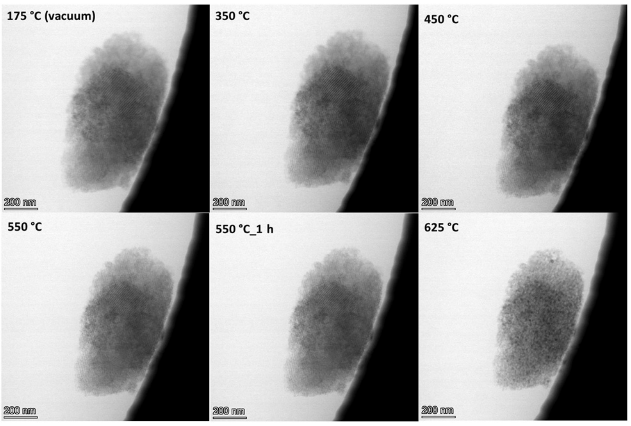

Fig. 8 Growth of MnO_x nano particles in a TEM (200 kV). Temperature from the start of the irradiation is displayed on each image. Diffusion of MnO_x on the surface is seen. Beam current density: 200 A cm^{-2}. Each image represents an area of 9.2 × 9.2 nm^2.

To validate and understand the particle growth phenomenon, we elevated the temperature to 625 °C. This additional temperature increment was chosen to confirm and observe any subsequent changes in MnO_x particles.

In Fig. S2 (ESI†), we examined the particle growth under a specific temperature condition of 550 °C. To capture the potential evolution of MnO_x crystals, we conducted a series of sequential imaging experiments at a slightly higher temperature, namely 625 °C. The imaging sessions were performed at specific intervals of 15 minutes, 45 minutes, 1 hour and 45 minutes, 2 hours and 45 minutes, and finally, 3 hours and 15 minutes. This approach aimed to assess whether MnO_x crystals exhibit growth at 550 °C over an extended duration.

Across all TEM image frames obtained from sequential imaging sessions, a consistent observation emerges: there is no discernible evidence of particle growth at 550 °C even when subjected to prolonged durations. This absence of observable growth underlines the stability and resistance of MnO_x crystals to significant changes in size or morphology under the specified temperature conditions.

Fig. S3 (ESI†) presents *in situ* validation of the growth and sintering behavior of MnO_x particles. TEM images were captured at a temperature of 625 °C for varying durations (5, 30, and 60 minutes) to observe the sintering behavior of the particles. Upon analysis of both STEM and TEM images (top and bottom, respectively), MnO_x nanoclusters are apparent on the SBA-15 surface. The particle size increased with time from 6 nm at 5 min to 14.5 nm at 60 min (see Fig. S4, ESI†). This result is consistent with the *ex situ* results of spent catalyst at 625 °C, where in both cases the average particle size increases with temperature. It is worth noting that due to the limited resolution of STEM imaging in *in situ* gas conditions, the clear identification of MnO_x particles is very difficult. Moreover, due to the sample thickness and complex morphology, even small changes in focus/astigmatism can disrupt the image of small

Mn oxide particles or it may highlight some defects in the SBA-15 structure that could be mistakenly identified as highly contrasted Mn oxide particles.

The resistance to sintering, as evidenced by the images, provides valuable insights into the robust nature of MnO_x particles within the SBA-15 framework. These observations contribute to our understanding of the thermal stability and behavior of MnO_x particles under the specific conditions explored in this study.

From Fig. 8 and Fig. S2 and S3 (ESI†) it is evident that there is diffusion of MnO_x particles emerging on the surface and migrating from the edges to the center. This observation is consistent with the recorded video Video S1 (ESI†) showing Mn migration across the surface with temperature elevation from 350 to 650 °C. We postulate that the facilitated Mn migration is due to the presence of P-123 in accordance with its proposed role in enhancing metal dispersion.[31,45,46]

X-ray photoelectron spectroscopy (XPS) was conducted to elucidate the surface chemical state of manganese (Mn). The atomic concentration of elements on the surfaces of 20Mn/SBA-15_d and 20Mn/SBA-15_w samples obtained by XPS are given in Table 2.

As shown in Fig. 9, high-resolution XPS spectra of Mn 2p core level was acquired for both samples. Subsequently, spectral deconvolution was employed to fit Mn $2p_{3/2}$ spectrum, using a combination of the standard references, namely MnO_2, Mn_2O_3, and MnO.[52] Notably, the results revealed the absence of MnO_2 in both samples. In the case of 20Mn/SBA-15_d catalyst, the presence of manganese was determined to be primarily in the form of Mn^{3+} oxides, whereas in the 20Mn/SBA-15_w sample, manganese was found to exist in a combination of Mn^{3+} and Mn^{2+} oxidation states. The utilization of the wet impregnation method thus resulted in a significant reduction in the concentration of Mn_2O_3 to 69%.

Table 2 Atomic concentration of elements on the surfaces of 20Mn/SBA-15_d and 20Mn/SBA-15_w samples obtained by XPS

Catalyst (s)	C 1s	O 1s	Si 2p	Mn 2p
20Mn/SBA-15_w	10.67	57.37	30.82	1.14
20MnO/SBA-15_d	7.48	59.55	29.56	3.41

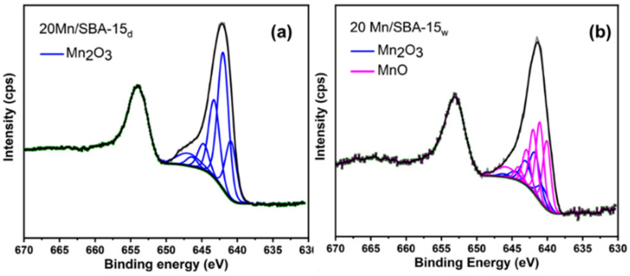

Fig. 9 XPS spectra of Mn 2p of (a) 20Mn/SBA-15_d and (b) 20Mn/SBA-15_w catalysts.

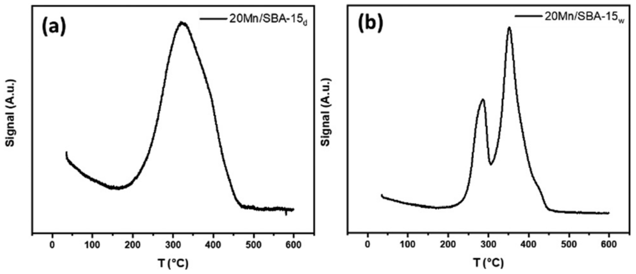

Fig. 10 H_2-TPR profile of 20Mn/SBA-15 catalyst prepared by (a) dry impregnation, and (b) wet impregnation.

To investigate bulk redox properties, H_2-TPR profiles of 20Mn/SBA-15_d and 20Mn/SBA-15_w were recorded (see Fig. 10). The reduction process of MnO_x into MnO by H_2 is reported over the temperature range of 200–550 °C.[56,57] This reduction pattern is observed in both cases of 20Mn/SBA-15_d and 20Mn/SBA-15_w. The 20Mn/SBA-15_d H_2 evolution showed a broad peak centered at 336 °C, which can be assigned to the highly dispersed MnO_x (as shown in XRD and TEM results).[58] The 20Mn/SBA-15_w catalysts showed two consecutive reduction peaks at 285 °C and 352 °C and a narrow peak shoulder at 412 °C. Jacob *et al.*[59] discovered that Mn_3O_4 is the main intermediate reduction product, the lower-temperature peak was ascribed to the reduction of MnO_2/Mn_2O_3 to Mn_3O_4, and the higher-temperature peak is attributed to the further reduction of Mn_3O_4 to MnO. The two-stage reduction pattern in the case of wet impregnated sample indicates more heterogeneity in the manganese species compared to the dry method.

The bulk average oxidation state from H_2-TPR is calculated based on the metal loading and hydrogen consumption assuming the reduction of all Mn species into MnO with Mn_2O_3.[56,57,60] Hydrogen consumption and average oxidation state for each sample are reported in Table 3. These findings align with our observations in the context of XPS measurements, suggesting coherence between surface and bulk properties of the MnO_x in the synthesized samples. The higher oxidation state in the case of dry impregnated sample is attributed to the enhanced oxygen uptake by smaller nanocrystals, as the oxidation rate is proportional to the surface to volume ratio.[61–63]

Fig. 11 shows the conversion profiles of ethylene using SBA-15 with different manganese loadings. By increasing the metallic loading from 10 to 20 wt%, the light-off temperature is shifted to lower temperatures by ∼100 °C. Catalyst activity decreases with further increase of metal content as observed with 25 and 30 wt% Mn/SBA-15 in dry impregnation. This trend

Table 3 Mn average oxidation state of 20Mn/SBA-15_d and 20Mn/SBA-15_w samples obtained by XPS and H_2-TPR

Catalyst (s)	Mn_2O_3 (%)	MnO (%)	Average oxidation state XPS	H_2 consumption (mmol g^{-1})	Average oxidation state H_2-TPR
20Mn/SBA-15_w	31	69	2.31	2.64	2.45
20Mn/SBA-15_d	98	2	2.98	3.53	2.94

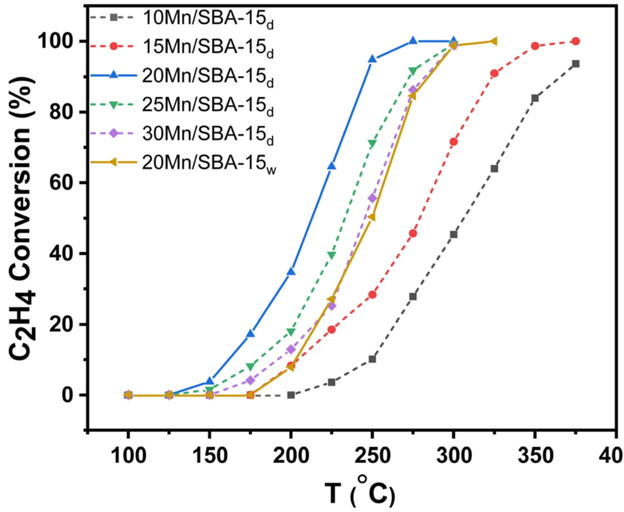

Fig. 11 Temperature screening of C_2H_4 oxidation on supported MnO_x/SBA-15 catalysts at a space velocity of 64 000 ml g_{cat}^{-1} h^{-1}.

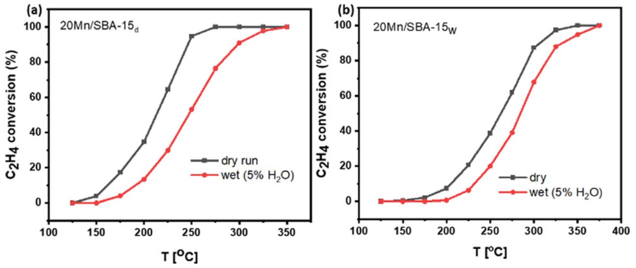

Fig. 12 Catalytic activity tests of MnO_x catalysts at GHSV of 64 000 ml g_{cat}^{-1} h^{-1} in dry and wet conditions; (a) 20Mn/SBA-15_d and (b) 20Mn/SBA-15_w. Test conducted with 850 ppm ethylene, 15% O_2, 5% H_2O (wet conditions) and balance N_2 at 250 °C.

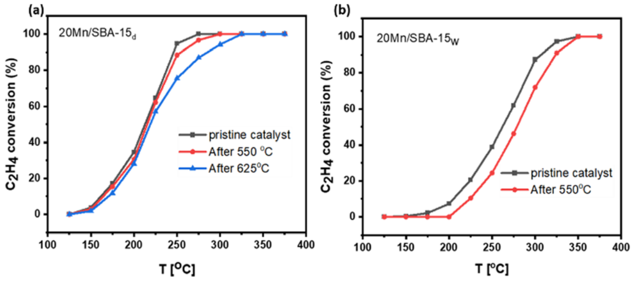

Fig. 13 Thermal stability evaluation of catalyst: (a) 20Mn/SBA-15_d (b) 20Mn/SBA-15_w.

suggests the onset of metal agglomeration, resulting in a reduction in the number of available active sites. The normalized conversion per Mn loading is shown in Fig. S5 (ESI†). The observed trend of increased activity with particle size growth in the 5–10 nm range aligns with the enhanced catalytic performance typically seen in transition metal oxide-based catalysts during redox reactions. Beyond this particle size range, the reduction in surface-to-volume ratio becomes dominant, leading to a decline in activity.[64,65] In this study, MnO_x did not exhibit well defined crystalline peaks in XRD pattens for Mn loadings below 20%, and TEM images did not reveal any observable surface nano particles at these loadings. However, at 20% Mn lading, MnO_x nanoparticles within the postulated optimum size range (5–10 nm) were observed in XRD pattens corresponding to crystalline MnO_x phases. Turn over frequency (TOF) values as a function of temperature are reported in Fig. S6 (ESI†); the results confirm the observed activity trends in Fig. S5 (ESI†) below 250 °C. The T_{90} value of 20Mn/SBA-15_d is 250 °C while that of 20Mn/SBA-15_w is 300 °C. This difference in performance could be attributed to the enhanced dispersion in the case of dry impregnated catalyst along with the higher average oxidation state. Shaheen *et al.*[66] reported decrease in activity with increased crystallinity, which is in accordance with our observation where wet impregnated sample has more pronounced XRD peaks due to the agglomeration of MnO_x nanoparticles. Another factor that explains the enhanced catalytic performance of dry impregnated catalysts is related to the abundance of Mn_2O_3 phases as quantified from XPS surface species. Mn_2O_3 phase in MnO_x is considered to be a highly desirable phase in oxidation reactions.[67,68]

The best performing catalyst activity in this work exhibits superior catalytic activity to several manganese-based catalyst for ethylene catalytic combustion. The activity is compared with literature results in Table 4 on the basis of the apparent rate constant (k [atm^{-2} s^{-1} g^{-1}]) at 150 °C.

To evaluate the performance of synthesized catalyst under wet conditions (which represent more realistic scenarios for VOC catalytic combustion),[15,51] conversion profiles are presented in Fig. 12. These profiles show that the catalytic activity of the dry impregnated catalyst surpasses that of its wet impregnated counterpart, with T_{90} values of 300 °C and 333 °C for dry and wet impregnated catalysts, respectively.

Thermal stability catalytic testing (Fig. 13) shows that the dry impregnated catalyst activity is maintained at 550 °C, while that

Table 4 Rate constant values at 150 °C for various Mn-based catalysts

Catalyst	Conditions	k [mol atm^{-1} s^{-1} g^{-1}]	Ref.
Mn_2O_3	500 ppm C_2H_4, 10% O_2, GHSV = 22 000 ml g^{-1} h^{-1}	1.4×10^{-5}	4[a]
$Fe_3Mn_1Cu_1O_x$	165 ppm C_2H_4, 10% O_2, GHSV = 60 000 ml g^{-1} h^{-1}	No conversion reported	69
Mn_3O_4	1000 ppm C_2H_4, 10% O_2, GHSV = 30 000 ml g^{-1} h^{-1}	1.13×10^{-5}	70
$MnCu_{7.5}Fe_{7.5}$	500 ppm C_2H_4, 10% O_2, GHSV = 20 000 ml g^{-1} h^{-1}	1.93×10^{-5}	71
Mn_2O_3-SG550	500 ppm C_2H_4, 10% O_2, GHSV = 22 730 ml g^{-1} h^{-1}	2.2×10^{-5}	72
$Ce_{55}Mn_{45}$-SiC	500 ppm C_2H_4, 10% O_2, GHSV = 15 400 ml g^{-1} h^{-1}	9.8×10^{-6}	3
20Mn/SBA-15_d	850 ppm C_2H_4, 15% O_2, GHSV = 64 000 ml g^{-1} h^{-1}	3.04×10^{-5}	This work

[a] Conversion values were reported at 160 °C instead of 150 °C.

of wet impregnated catalyst drops after the exposure to the same condition. This shows the higher thermal stability of dry impregnated sample. However, at 625 °C the activity of the dry impregnated sample drops significantly. These results are in accordance with the TEM findings where the catalyst deactivation is correlated to particle growth. The dry impregnated catalyst exhibited a stable catalytic performance at 225 °C, as shown in Fig. S7 (ESI†). These results are consistent with the recyclability assessments, where the light-on run showed no significant difference compared to the light-off conversion profiles, as shown in Fig. S8 (ESI†).

4. Conclusions

This study investigated the utilization of nanoconfinement effects facilitated by as-synthesized SBA-15 to disperse MnO_x nanoparticles within its channels. The controlled synthesis resulted in highly dispersed MnO_x nanoparticles with a size of ∼7.3 nm and a loading content of up to 30 wt%. With the med-synthesis approach, nanoconfinement in dry impregnation allowed particles to disperse on the inner surface of SBA-15, while maintaining an undecorated surface of SBA-15 surrounding each nanoparticle. MnO_x nanoparticles served as active sites for the oxidation of ethylene.

The choice between dry and wet impregnation methods for preparing Mn/SBA-15 catalyst significantly influences its catalytic performance and thermal stability in ethylene combustion. The observed variations in ethylene conversion rates and temperature dependencies highlight the importance of the preparation method in tailoring catalyst properties for specific applications. In comparison to MnO_x deposited through conventional wet impregnation, the nanoconfined catalyst exhibited superior performance. *In situ* TEM studies provided insights into the growth behavior of the nanoparticles, highlighting their stability and uniform distribution within the SBA-15 channels. Furthermore, our investigation revealed significant advantages of the nanoconfinement approach in terms of catalytic activity. Specifically, the oxidation of C_2H_4 exhibited a lower T_{90} temperature (250 °C) with the nanoconfinement catalyst compared to the catalyst synthesized using wet impregnation (T_{90} = 300 °C). The temperature investigation, along with EDX color mapping, provided valuable information on the dispersion and growth behavior of MnO_x nanoparticles at elevated temperatures. These findings demonstrate the potential of the nanoconfinement approach using SBA-15 for the development of efficient catalytic systems based on MnO_x nanoparticles.

Our study highlights the successful synthesis and characterization of nanoconfined MnO_x nanoparticles within SBA-15. The results emphasize the advantages of the nanoconfinement approach in terms of particle size control, dispersion, and catalytic performance. Further research and optimization of the nanoconfinement strategy could unlock new opportunities for the design and development of advanced catalysts for various applications.

Author contributions

Mohamad Abou-Daher: conceptualization, formal analysis, investigation, data curation, writing – original draft. Hassnain Abbas Khan: methodology, investigation, data curation, writing – original draft. Georgian Melinte: characterization and post reaction processing. Sarah Komaty: formal analysis, investigation, data curation.: formal analysis. Javier Ruiz-Martinez: supervision, writing – review & editing. Aamir Farooq: supervision, writing – review & editing, funding.

Data availability

The data supporting this article have been included as part of the ESI.†

Conflicts of interest

The authors declare no conflicts of interest.

Acknowledgements

This work was supported by funding from King Abdullah University of Science and Technology (KAUST) *via* the Competitive Research Grant # URF-3402.

References

1 S. Li, D. Wang, X. Wu and Y. Chen, Recent advance on VOCs oxidation over layered double hydroxides derived mixed metal oxides, *Chin. J. Catal.*, 2020, **41**, 550–560.

2 M. Monai, T. Montini, R. J. Gorte and P. Fornasiero, Catalytic Oxidation of Methane: Pd and Beyond, *Eur. J. Inorg. Chem.*, 2018, 2884–2893.

3 M. J. Marin Figueredo, T. Andana, S. Bensaid, M. Dosa, D. Fino, N. Russo and M. Piumetti, Cerium–Copper–Manganese Oxides Synthesized via Solution Combustion Synthesis (SCS) for Total Oxidation of VOCs, *Catal. Lett.*, 2020, **150**, 1821–1840.

4 C. Cocuzza, E. Sartoretti, C. Novara, F. Giorgis, S. Bensaid, N. Russo, D. Fino and M. Piumetti, Copper–manganese oxide catalysts prepared by solution combustion synthesis for total oxidation of VOCs, *Catal. Today*, 2023, **423**, 114292.

5 L. Elsgaard, Ethylene Removal at Low Temperatures under Biofilter and Batch Conditions, *Appl. Environ. Microbiol.*, 2000, **66**, 3878–3882.

6 R. Impens, Automotive Traffic Risks for the Environment, *Stud. Surf. Sci. Catal.*, 1987, **30**, 11–29.

7 G. Mabilon, D. Durand and P. H. Courty, Inhibition of post-combustion catalysts by alkynes: A clue for understanding their behaviour under real exhaust conditions, *Stud. Surf. Sci. Catal.*, 1995, **96**, 775–788.

8 J. M. A. Harmsen, J. H. B. J. Hoebink and J. C. Schouten, Transient Kinetic Modeling of the Ethylene and Carbon Monoxide Oxidation over a Commercial Automotive

Exhaust Gas Catalyst, *Ind. Eng. Chem. Res.*, 2000, **39**, 599–609.

9 Y. Guo, M. Wen, G. Li and T. An, Recent advances in VOC elimination by catalytic oxidation technology onto various nanoparticles catalysts: a critical review, *Appl. Catal., B*, 2021, **281**, 119447.

10 J. E. Lee, Y. S. Ok, D. C. W. Tsang, J. H. Song, S. C. Jung and Y. K. Park, Recent advances in volatile organic compounds abatement by catalysis and catalytic hybrid processes: a critical review, *Sci. Total Environ.*, 2020, **719**, 137405.

11 X. Mu, H. Ding, W. Pan, Q. Zhou, W. Du, K. Qiu, J. Ma and K. Zhang, Research progress in catalytic oxidation of volatile organic compound acetone, *J. Environ. Chem. Eng.*, 2021, **9**, 105650.

12 B. Lou, N. Shakoor, M. Adeel, P. Zhang, L. Huang, Y. Zhao, W. Zhao, Y. Jiang and Y. Rui, Catalytic oxidation of volatile organic compounds by non-noble metal catalyst: current advancement and future prospectives, *J. Cleaner Prod.*, 2022, **363**, 132523.

13 M. R. Morales, B. P. Barbero and L. E. Cadús, Total oxidation of ethanol and propane over Mn–Cu mixed oxide catalysts, *Appl. Catal., B*, 2006, **67**, 229–236.

14 S. S. Satter, T. Yokoya, J. Hirayama, K. Nakajima and A. Fukuoka, Oxidation of Trace Ethylene at 0 °C over Platinum Nanoparticles Supported on Silica, *ACS Sustainable Chem. Eng.*, 2018, **6**, 11480–11486.

15 H. A. Khan, M. Abou-Daher, A. L. S. de Freitas, J. Subburaj, O. E. Tall and A. Farooq, Performance studies of Pt, Pd and PtPd supported on SBA-15 for wet CO and hydrocarbon oxidation, *Catal. Today*, 2024, **426**, 114370.

16 M. J. Hazlett and W. S. Epling, Spatially resolving CO and C_3H_6 oxidation reactions in a Pt/Al_2O_3 model oxidation catalyst, *Catal. Today*, 2016, **267**, 157–166.

17 C. Jiang, K. Hara and A. Fukuoka, Low-temperature oxidation of ethylene over platinum nanoparticles supported on mesoporous silica, *Angew. Chem., Int. Ed.*, 2013, **52**, 6265–6268.

18 P. Jodłowski, R. Jędrzejczyk, D. Chlebda, A. Dziedzicka, Ł. Kuterasiński, A. Gancarczyk and M. Sitarz, Non-Noble Metal Oxide Catalysts for Methane Catalytic Combustion: Sonochemical Synthesis and Characterisation, *Nanomaterials*, 2017, **7**, 174.

19 P. Gélin and M. Primet, Complete oxidation of methane at low temperature over noble metal based catalysts: a review, *Appl. Catal., B*, 2002, **39**, 1–37.

20 M. Baldi, E. Finocchio, F. Milella and G. Busca, Catalytic combustion of C_3 hydrocarbons and oxygenates over Mn_3O_4, *Appl. Catal., B*, 1998, **16**, 43–51.

21 S. C. Kim, The catalytic oxidation of aromatic hydrocarbons over supported metal oxide, *J. Hazard. Mater.*, 2002, **91**, 285–299.

22 M. Baldi, V. S. Escribano, J. M. G. Amores, F. Milella and G. Busca, Characterization of manganese and iron oxides as combustion catalysts for propane and propene, *Appl. Catal., B*, 1998, **17**, L175–L182.

23 Y.-F. Han, F. Chen, Z. Zhong, K. Ramesh, L. Chen and E. Widjaja, Controlled synthesis, characterization, and catalytic properties of Mn(2)O(3) and Mn(3)O(4) nanoparticles supported on mesoporous silica SBA-15, *J. Phys. Chem. B*, 2006, **110**, 24450–24456.

24 Y. Yin, Z. F. Yang, Z. H. Wen, A. H. Yuan, X. Q. Liu, Z. Z. Zhang and H. Zhou, Modification of as Synthesized SBA-15 with Pt nanoparticles: Nanoconfinement Effects Give a Boost for Hydrogen Storage at Room Temperature, *Sci. Rep.*, 2017, **7**, 1–10.

25 F. Subhan, S. Aslam, Z. Yan, M. Yaseen, M. Naeem and A. Khan, Confinement of Au, Pd and Pt nanoparticle with reduced sizes: significant improvement of dispersion degree and catalytic activity, *Microporous Mesoporous Mater.*, 2022, **337**, 111927.

26 Y. Zhang, X. Li, Y. Zhang, T. Jiao, H. Zhang, W. Zhang and P. Liang, Mn(CeZr)Ox chelation-induced synthesis and its hydrothermal aging characteristics for catalytic abatement of toluene, *Chemosphere*, 2022, **288**, 132662.

27 H. A. Khan, J. Hao, O. El Tall and A. Farooq, Yttrium stabilization and Pt addition to Pd/ZrO_2 catalyst for the oxidation of methane in the presence of ethylene and water, *RSC Adv.*, 2021, **11**, 11910–11917.

28 D. Zhao, Triblock Copolymer Syntheses of Mesoporous Silica with Periodic 50 to 300 Angstrom Pores, *Science*, 1998, **279**, 548–552.

29 R. Nava, C. L. P. Ledesma, J. L. Romero and G. A. Nú, SBA-15 Mesoporous Silica as Catalytic Support for Hydrodesulfurization Catalysts—Review, *Materials*, 2013, 4139–4167.

30 L. M. Yang, Y. J. Wang, G. S. Luo and Y. Y. Dai, Functionalization of SBA-15 mesoporous silica with thiol or sulfonic acid groups under the crystallization conditions, *Microporous Mesoporous Mater.*, 2005, **84**, 275–282.

31 J. Shen and C. Hess, Controlling the dispersion of ceria using nanoconfinement: application to CeO_2/SBA-15 catalysts for NH_3-SCR, *Mater. Adv.*, 2021, **2**, 7400–7412.

32 J. Fan, X. Niu, W. Teng, P. Zhang, W. Zhang and D. Zhao, Highly dispersed Fe–Ce mixed oxide catalysts confined in mesochannels toward low-temperature oxidation of formaldehyde, *J. Mater. Chem. A*, 2020, **8**, 17174–17184.

33 O. Daoura, G. Fornasieri, M. Boutros, N. El Hassan, P. Beaunier, C. Thomas, M. Selmane, A. Miche, C. Sassoye, O. Ersen, W. Baaziz, P. Massiani, A. Bleuzen and F. Launay, One-pot prepared mesoporous silica SBA-15-like monoliths with embedded Ni particles as selective and stable catalysts for methane dry reforming, *Appl. Catal., B*, 2021, **280**, 119417.

34 P. Hongmanorom, J. Ashok, S. Das, N. Dewangan, Z. Bian, G. Mitchell, S. Xi, A. Borgna and S. Kawi, Zr–Ce-incorporated Ni/SBA-15 catalyst for high-temperature water gas shift reaction: methane suppression by incorporated Zr and Ce, *J. Catal.*, 2020, **387**, 47–61.

35 Y. Kathiraser, J. Ashok and S. Kawi, Synthesis and evaluation of highly dispersed SBA-15 supported Ni–Fe bimetallic catalysts for steam reforming of biomass derived tar reaction, *Catal. Sci. Technol.*, 2016, **6**, 4327–4336.

36 J. Zhu, Z. Ko, V. F. Puntes, I. Kiricsi, C. X. Miao, J. W. Ager, A. P. Alivisatos and G. A. Somorjai, Encapsulation of Metal (Au, Ag, Pt) Nanoparticles into the Mesoporous SBA-15 Structure, *Langmuir*, 2003, 4396–4401.

37 M. Tao, X. Meng, Y. Lv, Z. Bian and Z. Xin, Effect of impregnation solvent on Ni dispersion and catalytic properties of Ni/SBA-15 for CO methanation reaction, *Fuel*, 2016, **165**, 289–297.

38 S. Chytil, W. R. Glomm and E. A. Blekkan, Characterization of Pt/SBA-15 prepared by the deposition-precipitation method, *Catal. Today*, 2009, **147**, 217–223.

39 A. Zukal, H. Siklová and J. Cejka, Grafting of alumina on SBA-15: effect of surface roughness, *Langmuir*, 2008, **24**, 9837–9842.

40 W. Tang, X. Wu and Y. Chen, Catalytic removal of gaseous benzene over Pt/SBA-15 catalyst: the effect of the preparation method, *React. Kinet., Mech. Catal.*, 2015, **114**, 711–723.

41 J. Kruatim, S. Jantasee and B. Jongsomjit, Improvement of cobalt dispersion on Co/SBA-15 and Co/SBA-16 catalysts by ultrasound and vacuum treatments during post-impregnation step, *Eng. J.*, 2017, **21**, 17–28.

42 H. A. Khan, A. Jaleel, P. Natarajan, S. Yoon and K.-D. Jung, Pt stabilization on Pt/SBA-15 through surface modification using MPTMS for sulfuric acid decomposition in SI cycle to produce hydrogen, *Int. J. Hydrogen Energy*, 2020, **45**(10), 5772–5782.

43 Y. Yin, D. M. Xue, X. Q. Liu, G. Xu, P. Ye, M. Y. Wu and L. B. Sun, Unusual ceria dispersion formed in confined space: a stable and reusable adsorbent for aromatic sulfur capture, *Chem. Commun.*, 2012, **48**, 9495–9497.

44 Y. M. Wang, Z. Y. Wu, L. Y. Shi and J. H. Zhu, Rapid functionalization of mesoporous materials: directly dispersing metal oxides into as-prepared SBA-15 occluded with template, *Adv. Mater.*, 2005, **17**, 323–327.

45 Y. Yin, Z.-H. Wen, X.-Q. Liu, A.-H. Yuan and L. Shi, Functionalization of SBA-15 with CeO_2 nanoparticles for adsorptive desulfurization: matters of template P123, *Adsorpt. Sci. Technol.*, 2018, **36**, 953–966.

46 Y. Yin, H. Wu, L. Shi, J. Zhang, X. Xu, H. Zhang, S. Wang, M. Sillanpääd and H. Sun, Quasi single cobalt sites in nanopores for superior catalytic oxidation of organic pollutants, *Environ. Sci.: Nano*, 2018, **5**, 2842–2852.

47 J. Zhu, X. Xie, S. A. C. Carabineiro, P. B. Tavares, J. L. Figueiredo, R. Schomäcker and A. Thomas, Facile one-pot synthesis of Pt nanoparticles/SBA-15: an active and stable material for catalytic applications, *Energy Environ. Sci.*, 2011, **4**, 2020.

48 G. J. Kim, D. W. Kwon and S. C. Hong, Effect of Pt Particle Size and Valence State on the Performance of Pt/TiO_2 Catalysts for CO Oxidation at Room Temperature, *J. Phys. Chem. C*, 2016, **120**, 17996–18004.

49 N. Radic, B. Grbic and A. Terlecki-Baricevic, Kinetics of deep oxidation of *n*-hexane and toluene over Pt/Al_2O_3 catalysts, *Appl. Catal., B*, 2004, **50**, 153–159.

50 R. J. Isaifan, S. Ntais and E. A. Baranova, Particle size effect on catalytic activity of carbon-supported Pt nanoparticles for complete ethylene oxidation, *Appl. Catal., A*, 2013, **464–465**, 87–94.

51 H. A. Khan, A. Jaleel, P. Natarajan, S. Yoon and K.-D. Jung, Pt stabilization on Pt/SBA-15 through surface modification using MPTMS for sulfuric acid decomposition in SI cycle to produce hydrogen, *Int. J. Hydrogen Energy*, 2020, **45**, 5772–5782.

52 M. C. Biesinger, B. P. Payne, A. P. Grosvenor, L. W. M. Lau, A. R. Gerson and R. S. C. Smart, Resolving surface chemical states in XPS analysis of first row transition metals, oxides and hydroxides: Cr, Mn, Fe, Co and Ni, *Appl. Surf. Sci.*, 2011, **257**, 2717–2730.

53 A. G. Gebretatios, F. Banat, T. Witoon and C. K. Cheng, Synthesis of sustainable rice husk ash-derived nickel-decorated MCM-41 and SBA-15 mesoporous silica materials for hydrogen storage, *Int. J. Hydrogen Energy*, 2024, **51**, 255–266.

54 H. Liang, K. Chai, F. Shen, H. He, G. He, C. Chen and Z. Wei, Methylthiazole Schiff base functionalized SBA-15 for high-performance Pb(II) capture and separation, *Microporous Mesoporous Mater.*, 2023, **351**, 112476.

55 M. Ding, J. Tu, J. Liu, N. Tsubaki, T. Wang and L. Ma, Copper–iron supported bimodal pore catalyst and its application for higher alcohols synthesis, *Catal. Today*, 2014, **234**, 278–284.

56 S. Komaty, M. Andijani, N. Wang, J. C. Navarro de Miguel, S. Kumar Veeranmaril, M. N. Hedhili, C. I. Q. Silva, Y. Wang, M. Abou-Daher, Y. Han and J. Ruiz-Martinez, Enhancing Water Tolerance and N_2 Selectivity in NH_3-SCR Catalysts by Protecting Mn Oxide Nanoparticles in a Silicalite-1 Layer, *Environ. Sci. Technol.*, 2024, **58**(34), 14963–15354.

57 L. E. Gevers, L. R. Enakonda, A. Shahid, S. Ould-Chikh, C. I. Q. Silva, P. P. Paalanen, A. Aguilar-Tapia, J.-L. Hazemann, M. N. Hedhili, F. Wen and J. Ruiz-Martínez, Unraveling the structure and role of Mn and Ce for NO_x reduction in application-relevant catalysts, *Nat. Commun.*, 2022, **13**, 2960.

58 I. Song, S. Youn and D. H. Kim, Characteristics of Manganese Supported on Hydrous Titanium Oxide Catalysts for the Selective Catalytic Reduction of NO_x with Ammonia, *Top. Catal.*, 2016, **59**, 1008–1012.

59 K. T. Jacob, A. Kumar, G. Rajitha and Y. Waseda, Thermodynamic data for Mn_3O_4, Mn_2O_3 and MnO_2, *High Temp. Mater. Processes*, 2011, **30**, 459–472.

60 D. Chlala, J.-M. Giraudon, N. Nuns, C. Lancelot, R.-N. Vannier, M. Labaki and J.-F. Lamonier, Active Mn species well dispersed on Ca^{2+} enriched apatite for total oxidation of toluene, *Appl. Catal., B*, 2016, **184**, 87–95.

61 C. Reed, Y.-K. Lee and S. T. Oyama, Structure and Oxidation State of Silica-Supported Manganese Oxide Catalysts and Reactivity for Acetone Oxidation with Ozone, *J. Phys. Chem. B*, 2006, **110**, 4207–4216.

62 H. Antoni, W. Xia, J. Masa, W. Schuhmann and M. Muhler, Tuning the oxidation state of manganese oxide nanoparticles on oxygen- and nitrogen-functionalized carbon nanotubes for the electrocatalytic oxygen evolution reaction, *Phys. Chem. Chem. Phys.*, 2017, **19**, 18434–18442.

63 Z.-W. Chen, S.-Y. Zhang, S. Tan, J. Wang and S.-Z. Jin, Different aspects of the microstructure of nanometer-sized Mn_2O_3, *Mater. Res. Bull.*, 1999, **34**, 1583–1587.

64 P. van Helden, I. M. Ciobîcă and R. L. J. Coetzer, The size-dependent site composition of FCC cobalt nanocrystals, *Catal. Today*, 2016, **261**, 48–59.

65 M. Che and C. O. Bennett, The Influence of Particle Size on the Catalytic Properties of Supported Metals, *Adv. Catal.*, 1989, **36**, 55–172.

66 W. M. Shaheen and M. M. Selim, Effect of thermal treatment on physicochemical properties of pure and mixed manganese carbonate and basic copper carbonate, *Thermochim. Acta*, 1998, **322**, 117–128.

67 P. M. Shah, L. A. Bailey, D. J. Morgan and S. H. Taylor, The Effect of Metal Ratio and Precipitation Agent on Highly Active Iron-Manganese Mixed Metal Oxide Catalysts for Propane Total Oxidation, *Catalysts*, 2023, **13**(5), 794.

68 M. A. Peluso, J. E. Sambeth and H. J. Thomas, Complete Oxidation Of Ethanol Over MnO_x, *React. Kinet. Catal. Lett.*, 2003, **80**, 241–248.

69 C. H. Weng, C. Y. Liao, J. H. Tzeng, Y. C. Chen, J. Anotai and Y. T. Lin, Constructing oxygen vacancy induced Fe–Mn–Cu mixed oxides for efficient catalytic combustion of ethylene, *Appl. Surf. Sci.*, 2023, **631**, 157555.

70 M. Piumetti, D. Fino and N. Russo, Mesoporous manganese oxides prepared by solution combustion synthesis as catalysts for the total oxidation of VOCs, *Appl. Catal., B*, 2015, **163**, 277–287.

71 M. J. Marin Figueredo, M. Piumetti, S. Bensaid, D. Fino and R. Nunzio, *Nanostructured Catalysts for Environmental Applications*, Springer International Publishing, Cham, 2021, pp. 59–78.

72 M. J. M. Figueredo, C. Cocuzza, S. Bensaid, D. Fino, M. Piumetti and N. Russo, Catalytic Abatement of Volatile Organic Compounds and Soot over Manganese Oxide Catalysts, *Materials*, 2021, **14**, 4534.